Plane wave solution for elastic wave scattering by a heterogeneous fracture

Seiji Nakagawa,[a] Kurt T. Nihei, and Larry R. Myer
Earth Sciences Division, Lawrence Berkeley National Laboratory, Berkeley, California 94720

(Received 22 March 2003; revised 6 March 2004; accepted 15 March 2004)

A plane-wave method for computing the three-dimensional scattering of propagating elastic waves by a planar fracture with heterogeneous fracture compliance distribution is presented. This method is based upon the spatial Fourier transform of the seismic displacement-discontinuity (SDD) boundary conditions (also called linear slip interface conditions), and therefore, called the wave-number-domain SDD method (wd-SDD method). The resulting boundary conditions explicitly show the coupling between plane waves with an incident wave number component (specular component) and scattered waves which do not follow Snell's law (nonspecular components) if the fracture is viewed as a planar boundary. For a spatially periodic fracture compliance distribution, these boundary conditions can be cast into a linear system of equations that can be solved for the amplitudes of individual wave modes and wave numbers. We demonstrate the developed technique for a simulated fracture with a stochastic (correlated) surface compliance distribution. Low- and high-frequency solutions of the method are also compared to the predictions by low-order Born series in the weak and strong scattering limit. [DOI: 10.1121/1.1739483]

PACS numbers: 43.20.Gp, 43.20.Px, 43.58.Ta [LLT] Pages: 2761–2772

I. INTRODUCTION

At microscales, fractures in rocks, metals, and ceramics can take many different forms including aligned open cracks, two surfaces in imperfect contact and a planar, thin zone filled with materials more compliant than the background medium.[1] Since a fracture scatters propagating elastic waves as a function of the microscale structure and resulting mechanical properties, they can be detected and characterized from the scattering behavior of the waves. The microscale properties, including surface roughness and aperture distribution, and connectivity and permeability of the cracks and gouge material, can also have a large impact on the hydraulic properties of a fracture.

Unfortunately, the microscale geometry and spatial property variations of a fracture is difficult to resolve using elastic waves if these heterogeneous features are much smaller than the wavelengths. Instead, these heterogeneities are likely to affect the scattering behavior of the waves through static, effective mechanical properties of the fracture that are determined at some subwavelength scale larger than the heterogeneities themselves. This is one of the basic principles of the seismic displacement–discontinuity (SDD) boundary conditions (also known as linear-slip interface conditions) commonly used for examining elastic wave scattering by fractures.

The SDD conditions assume a linear relationship between the wave-introduced, small relative displacement and stress across a fracture, via material parameters called fracture stiffness and its inverse, fracture compliance.[2] Since the SDD model is incapable of discriminating the detailed local geometry of a fracture, the fracture compliance does not directly reflect the hydraulic properties. However, in general, a large compliance value suggests a more open, permeable fracture. Baik and Thompson (1984)[3] showed that the fracture compliance can be determined analytically for fractures consisting of sparsely distributed, co-planar circular cracks and of contact patches between half-spaces. Angel and Achenbach (1985)[4] showed that elastic wave scattering off a fracture, consisting of aligned microcracks, can be modeled by the SDD conditions for long wavelengths. From laboratory ultrasonic transmission tests across a synthetic fracture with known, regular geometry, Myer *et al.* (1985)[5] found good agreement between measured waves and theoretical prediction by the SDD model.

Theoretical studies based upon the SDD model on the elastic wave scattering by fractures are limited to, or assume, fractures with a homogeneous distribution of fracture compliance on the fracture plane.[2,6–8] This is because the conventional SDD model, when used with plane wave theory, requires a "range-independent" (material properties do not vary along the fracture plane) fracture compliance distribution. Naturally occurring fractures are, however, heterogeneous, with the microscale properties varying along the fracture plane. This gives rise to fracture compliance that is spatially heterogeneous and, possibly, correlated. Since the heterogeneity of a fracture has a great impact on the hydraulic and mechanical properties of the fracture,[9–12] understanding the effect of the heterogeneity on the scattering of elastic waves can provide valuable tools for geophysical and nondestructive characterization of the fracture properties.

In this paper, we present analytical and numerical techniques to examine the elastic wave scattering by a heterogeneous fracture, based on the "local" SDD boundary conditions and the plane wave theory. This is achieved by

[a]Author to whom correspondence should be addressed; electronic mail: snakagawa@lbl.gov

applying a spatial Fourier transform to the SDD conditions with "local" fracture compliance that is a function in space. For this reason, this method is called the wave number domain seismic displacement discontinuity method (wd–SDD method). Previously, the local SDD model was used in geometric ray approximations. Pyrak-Nolte and Nolte (1992)[13] examined the apparent, scattering induced frequency dependence of fracture compliance assuming that the compliance varied much more slowly compared to the wavelength (high-frequency ray approximation). Nihei (1989)[14] and Oliger *et al.* (2003)[15] used Kirchhoff approximations to take into account the diffraction of waves transmitted across a heterogeneous fracture. In the Kirchhoff approximations, the amplitudes and phases of the transmitted waves across a fracture are computed at each location on the fracture, assuming that the fracture is planar and has a single value of fracture compliance assigned to that location. In contrast, the wd–SDD method is not limited to high frequencies and takes into account the interactions between different locations on the fracture. Although numerical methods such as the boundary element method[16] and the finite difference method[17,18] can also be used to examine the scattering of elastic waves at full range of frequencies, applications of these methods to three-dimensional problems results in high computational costs, particularly large computer memory. Further, the analytical nature of the introduced method can provide clearer insights into the mechanism of wave scattering by a heterogeneous fracture.

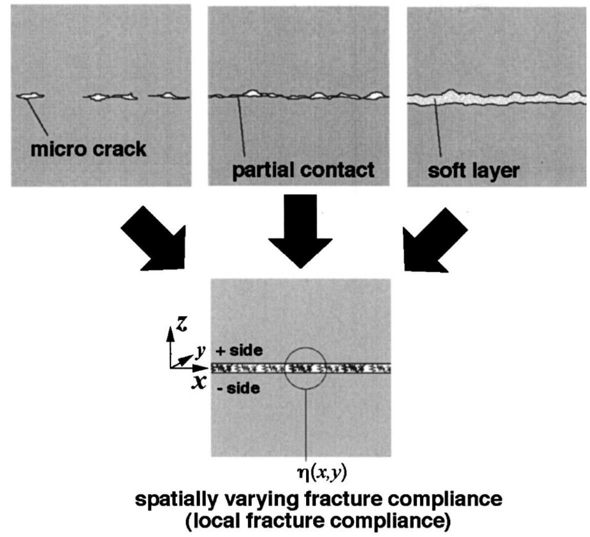

FIG. 1. Heterogeneous fractures with a variety of microstructures are modeled as a planer interface between half-spaces with spatially varying fracture compliance (springs in the figure).

II. THEORY

A. Plane wave analysis

We first hypothesize that the "local fracture compliance" can be defined for a fracture. This means that the dynamic behavior of a real fracture is well approximated by the behavior of an interface between half-spaces with a heterogeneous distribution of compliance which is measured locally at some length scale much smaller than the seismic (elastic wave) wavelengths. This approach is commonly taken to numerically simulate wave scattering by fractures with heterogeneous surface contacts using the boundary element method and the finite difference method.

In our model, we also assume that the dimension of a fracture in the fracture-normal direction, such as the surface roughness and waviness, is much smaller than considered seismic wavelengths, and therefore, the fracture can be treated as a plane. For the local fracture compliance model, the SDD boundary conditions are specified at each spatial location on the fracture on the x, y plane as (Fig. 1)

$$\boldsymbol{\sigma}(x,y;z\to+0)=\boldsymbol{\sigma}(x,y;z\to-0)\equiv\boldsymbol{\sigma}(x,y), \tag{1}$$

$$\boldsymbol{\eta}(x,y)\,\boldsymbol{\sigma}(x,y)=[\mathbf{u}](x,y), \tag{2}$$

where the displacement–discontinuity vector $[\mathbf{u}]$, stress traction vectors $\boldsymbol{\sigma}$, and the compliance matrix $\boldsymbol{\eta}$ are defined as

$$[\mathbf{u}](x,y)\equiv\mathbf{u}(x,y;z\to+0)-\mathbf{u}(x,y;z\to-0)$$
$$=\begin{bmatrix}u_x\\u_y\\u_z\end{bmatrix}_{z\to+0}-\begin{bmatrix}u_x\\u_y\\u_z\end{bmatrix}_{z\to-0}, \tag{3}$$

$$\boldsymbol{\sigma}(x,y;z\to\pm0)=\begin{bmatrix}\sigma_{xz}\\\sigma_{yz}\\\sigma_{zz}\end{bmatrix}_{z\to\pm0}, \tag{4}$$

$$\boldsymbol{\eta}(x,y)\equiv\begin{bmatrix}\eta_{xx}&\eta_{xy}&\eta_{xz}\\\eta_{yx}&\eta_{yy}&\eta_{yz}\\\eta_{zx}&\eta_{zy}&\eta_{zz}\end{bmatrix}. \tag{5}$$

It is noted that the stress traction vector is defined via components of stress on planes parallel to the x, y plane rather than components of traction the sign of which depends on the orientation of the surface. However, without confusion, we shall call this "traction (vector)." We assume that the incident waves insonify the fracture on the $z<0$ side. By directly applying the spatial 2D Fourier transform to these "local" SDD conditions given in Eqs. (1) and (2), we get

$$\tilde{\boldsymbol{\sigma}}(k_x,k_y;z\to+0)=\tilde{\boldsymbol{\sigma}}(k_x,k_y;z\to-0)\equiv\tilde{\boldsymbol{\sigma}}(k_x,k_y), \tag{6}$$

$$(\tilde{\boldsymbol{\eta}}*\tilde{\boldsymbol{\sigma}})(k_x,k_y)=[\tilde{\mathbf{u}}](k_x,k_y). \tag{7}$$

Tilde "~" indicates transformed variables, and "*" indicates a convolution. It is noted that for a uniform fracture, $\boldsymbol{\eta}(x,y)$ is a constant matrix, and the convolution is reduced to a multiplication, i.e., the same relationship as in the x, y domain.

In this paper, we assume a single plane fracture embedded within a homogeneous background medium with a stiffness tensor $\mathbf{C}=[C_{ijkl}]$ and a density ρ. For a given frequency ω and fracture-parallel wave numbers k_x and k_y, the Christoffel equation is solved to obtain six z-direction wave numbers $k_z^{1\pm}$, $k_z^{2\pm}$, $k_z^{3\pm}$, where 1, 2, 3 indicate the three modes of plane waves, and corresponding unit particle displacement vectors $\hat{\mathbf{u}}_1^{\pm}$, $\hat{\mathbf{u}}_2^{\pm}$, $\hat{\mathbf{u}}_3^{\pm}$. Hereafter, the superscripts

"$^-$" and "$^+$" indicate waves propagating in the negative z direction (reflected waves) and in the positive z direction (incident and transmitted waves), respectively. For plane waves, the displacement and stress can be related to each other via single vector variables $\mathbf{a}^{\pm}$ containing the displacement amplitudes of three plane wave modes. Using the wave numbers and unit displacement vectors defined in the above, a single wave number component of the plane wave displacement is given by

$$\mathbf{u}^{\pm}(x,y;z) = \begin{bmatrix} u_x^{\pm} \\ u_y^{\pm} \\ u_z^{\pm} \end{bmatrix} (=\tilde{\mathbf{u}}^{\pm}(k_x,k_y;z)) = \{\hat{\mathbf{u}}_1^{\pm} \quad \hat{\mathbf{u}}_2^{\pm} \quad \hat{\mathbf{u}}_3^{\pm}\} \times \begin{bmatrix} e^{ik_z^{1\pm}z} & & \\ & e^{ik_z^{2\pm}z} & \\ & & e^{ik_z^{3\pm}z} \end{bmatrix} \times \begin{bmatrix} a_1^{\pm} \\ a_2^{\pm} \\ a_3^{\pm} \end{bmatrix} e^{i(k_x x + k_y y - \omega t)} \equiv \mathbf{U}^{\pm}(k_x,k_y)\mathbf{E}^{\pm}(k_x,k_y;z)\mathbf{a}^{\pm}(k_x,k_y)e^{i(k_x x + k_y y - \omega t)}, \quad (8)$$

where ω is the circular frequency. The traction is computed from the displacement vector using the Hooke's law as

$$\boldsymbol{\sigma}^{\pm}(x,y;z)(=\tilde{\boldsymbol{\sigma}}^{\pm}(k_x,k_y;z)) = \begin{bmatrix} \sigma_{xz}^{\pm} \\ \sigma_{yz}^{\pm} \\ \sigma_{zz}^{\pm} \end{bmatrix} = i\omega\mathbf{S}^{\pm}(k_x,k_y)\mathbf{E}^{\pm}(k_x,k_y;z)\mathbf{a}^{\pm}(k_x,k_y)e^{i(k_x x + k_y y - \omega t)}. \quad (9)$$

Dependence on the phase term, $e^{i(k_x x + k_y y - \omega t)}$, is understood and omitted from the following equations. We will define $\mathbf{S}^{\pm}$ shortly.

For an isotropic background medium, the three modes of wave propagation are two shear (S) waves and one compressional (P) wave. We label these modes as $1=Sv$ wave, $2=Sh$ wave, and $3=P$ wave, where a convention is taken such that the Sh wave has the particle displacement parallel to the fracture (or z) plane. For a plane-parallel wave number $k_r=\sqrt{k_x^2+k_y^2}$, the z-direction wave numbers are $k_z^{1,2\pm}=\pm k_z^S \equiv \pm\sqrt{k_S^2-k_r^2}$ and $k_z^{3\pm}=\pm k_z^P \equiv \pm\sqrt{k_P^2-k_r^2}$, where $k_P=\omega/c_P$ and $k_S=\omega/c_S$ are the P- and S-wave wave numbers with velocities c_P and c_S, respectively. The displacement and stress matrices in Eqs. (8) and (9) take the forms

$$\mathbf{U}^{\pm} = \mathbf{R}^T \begin{bmatrix} \mp k_z^S/k_S & & k_r/k_P \\ & 1 & \\ k_r/k_S & & \pm k_z^P/k_P \end{bmatrix}, \quad (10)$$

$$\mathbf{S}^{\pm} = \rho c_S \mathbf{R}^T \begin{bmatrix} -(1-2(k_r/k_S)^2) & 0 & \pm 2k_r k_z^P/k_P k_S \\ 0 & \pm k_z^S/k_S & 0 \\ \pm 2k_r k_z^S/k_S^2 & 0 & (1-2(k_r/k_S)^2)(k_S/k_P) \end{bmatrix}, \quad (11)$$

where $\mathbf{R}$ is the rotation matrix around the z axis given by

$$\mathbf{R} \equiv \begin{bmatrix} k_x/k_r & k_y/k_r & \\ -k_y/k_r & k_x/k_r & \\ & & 1 \end{bmatrix}. \quad (12)$$

The superscript "^{T}" indicates matrix transposition. It is noted that the matrices $\mathbf{U}^{\pm}$ and $\mathbf{R}$ are dimensionless, and $\mathbf{S}^{\pm}$ has the dimension of acoustic impedance. Also, all of these matrices are frequency independent for a given wave propagation direction (or a fracture-parallel slowness) because wave numbers in the expressions appear only as a ratio between two wave numbers.

Using Eqs. (8) and (9), the displacement and traction introduced by an incident plane wave propagating in the positive z direction are $\tilde{\mathbf{u}}_{\mathrm{Inc}}=\mathbf{U}^+\mathbf{E}^+\mathbf{a}_{\mathrm{Inc}}$ and $\tilde{\boldsymbol{\sigma}}_{\mathrm{Inc}}=i\omega\mathbf{S}^+\mathbf{E}^+\mathbf{a}_{\mathrm{Inc}}$, respectively, where $\mathbf{a}_{\mathrm{Inc}}$ contains the displacement amplitudes of the individual plane wave modes. Using Eq. (8), and noting that there are no waves propagating in the negative z direction on the $z>0$ side of the fracture, the transformed-domain displacement–discontinuity vector on the fracture is computed from Eqs. (3), (8), and (10) as

$$[\tilde{\mathbf{u}}] \equiv \tilde{\mathbf{u}}(z\to+0) - \tilde{\mathbf{u}}(z\to-0) = [\tilde{\mathbf{u}}^+ - (\tilde{\mathbf{u}}^- + \tilde{\mathbf{u}}_{\mathrm{Inc}})]_{z=0} = \mathbf{U}^+\mathbf{a}^+ - (\mathbf{U}^-\mathbf{a}^- + \mathbf{U}^+\mathbf{a}_{\mathrm{Inc}}). \quad (13)$$

The traction vectors are given by Eqs. (9) and (11) as

$$\tilde{\boldsymbol{\sigma}}(z\to+0) = (\tilde{\boldsymbol{\sigma}}^+)_{z=0} = i\omega\mathbf{S}^+\mathbf{a}^+,$$
$$\tilde{\boldsymbol{\sigma}}(z\to-0) = (\tilde{\boldsymbol{\sigma}}^- + \tilde{\boldsymbol{\sigma}}_{\mathrm{Inc}})_{z=0} = i\omega(\mathbf{S}^-\mathbf{a}^- + \mathbf{S}^+\mathbf{a}_{\mathrm{Inc}}). \quad (14)$$

Using Eqs. (13) and (14), Eqs. (6) and (7) are rewritten, respectively, as

$$i\omega\mathbf{S}^+\mathbf{a}^+ = i\omega(\mathbf{S}^-\mathbf{a}^- + \mathbf{S}^+\mathbf{a}_{\mathrm{Inc}}) \equiv \tilde{\boldsymbol{\sigma}}(k_x,k_y), \quad (15)$$

$$\tilde{\boldsymbol{\eta}}^*(i\omega\mathbf{S}^+\mathbf{a}^+) = \mathbf{U}^+\mathbf{a}^+ - \mathbf{U}^-\mathbf{a}^- - \mathbf{U}^+\mathbf{a}_{\mathrm{Inc}}. \quad (16)$$

To simplify the above equations, we choose to use the traction vector $\tilde{\boldsymbol{\sigma}}$ as our primary variable. This choice leads to an efficient implementation of a numerical algorithm, which we will discuss later. Using the equalities in the first equation,

$$\mathbf{a}^{+}=(i\omega\mathbf{S}^{+})^{-1}\tilde{\boldsymbol{\sigma}},\qquad \mathbf{a}^{-}=(i\omega\mathbf{S}^{-})^{-1}(\tilde{\boldsymbol{\sigma}}-i\omega\mathbf{S}^{+}\mathbf{a}_{\mathrm{Inc}}). \tag{17}$$

These are used to eliminate the variables $\mathbf{a}^{-}$ and $\mathbf{a}^{+}$ from Eq. (16), resulting in

$$\begin{aligned}\tilde{\boldsymbol{\eta}}^{*}\tilde{\boldsymbol{\sigma}}&=\mathbf{U}^{+}(i\omega\mathbf{S}^{+})^{-1}\tilde{\boldsymbol{\sigma}}-\mathbf{U}^{-}(i\omega\mathbf{S}^{-})^{-1}(\tilde{\boldsymbol{\sigma}}-i\omega\mathbf{S}^{+}\mathbf{a}_{\mathrm{Inc}})\\&\quad-\mathbf{U}^{+}\mathbf{a}_{\mathrm{Inc}}\\&=(i\omega)^{-1}[\mathbf{U}^{+}(\mathbf{S}^{+})^{-1}-\mathbf{U}^{-}(\mathbf{S}^{-})^{-1}](\tilde{\boldsymbol{\sigma}}-i\omega\mathbf{S}^{+}\mathbf{a}_{\mathrm{Inc}})\\&\equiv(i\omega)^{-1}\mathbf{H}(\tilde{\boldsymbol{\sigma}}-\tilde{\boldsymbol{\sigma}}_{\mathrm{Inc}}).\end{aligned} \tag{18}$$

or

$$[(i\omega)^{-1}\mathbf{H}-\tilde{\boldsymbol{\eta}}^{*}]\tilde{\boldsymbol{\sigma}}=(i\omega)^{-1}\mathbf{H}\tilde{\boldsymbol{\sigma}}_{\mathrm{Inc}}. \tag{19}$$

Note that the stress introduced by the incident wave is evaluated on the fracture $(z=0)$. The matrix $\mathbf{H}$ is defined as

$$\begin{aligned}\mathbf{H}&\equiv\mathbf{U}^{+}(\mathbf{S}^{+})^{-1}-\mathbf{U}^{-}(\mathbf{S}^{-})^{-1}\\&=\frac{2}{\rho c_S\cdot R}\mathbf{R}^{T}\begin{bmatrix}k_z^S/k_S&&\\&k_SR/k_z^S&\\&&k_z^P/k_S\end{bmatrix}\mathbf{R},\end{aligned} \tag{20}$$

where R is the dimensionless Rayleigh function

$$R\equiv[1-2(k_r/k_S)^2]^2+4(k_r/k_S)^2(k_z^Pk_z^S/k_S^2). \tag{21}$$

It is noted that $\mathbf{H}$ has the dimension of inverse acoustic impedance, and both R and $\mathbf{H}$ are frequency independent for a fixed wave propagation direction.

Equation (19) is a Fredholm integral equation of the second kind for the total stress $\tilde{\boldsymbol{\sigma}}$ on the fracture, which can be given explicitly as

$$\begin{aligned}\tilde{\boldsymbol{\sigma}}(k_x,k_y)&=\tilde{\boldsymbol{\sigma}}_{\mathrm{Inc}}(k_x,k_y)+i\omega\mathbf{H}^{-1}(k_x,k_y)\\&\quad\times\int_{-\infty}^{+\infty}\int_{-\infty}^{+\infty}\tilde{\boldsymbol{\eta}}(k_x-k_x',k_y-k_y')\\&\quad\times\tilde{\boldsymbol{\sigma}}(k_x',k_y')\,dk_x'\,dk_y'.\end{aligned} \tag{22}$$

The first term on the right-hand side of the equation is the incident wave field, and the second term is the scattered wave field. The second term shows that, for a heterogeneous fracture compliance distribution, different wave number components are coupled through the convolution with the Fourier transformed fracture compliance, resulting in nonspecular transmission and reflection of an incident plane wave. For simplicity, we define 3×3 matrix operators $\overline{\mathbf{H}}^{-1}$ and $\bar{\tilde{\boldsymbol{\eta}}}$. $\overline{\mathbf{H}}^{-1}$ is a "diagonal" multiplication operator (performs multiplication by the matrix $\mathbf{H}^{-1}$), and $\bar{\tilde{\boldsymbol{\eta}}}$ is a convolution operator [performs convolution in Eq. (12) with multiplication by the matrix $\tilde{\boldsymbol{\eta}}$]. The formal solution of Eq. (22) is obtained (Neumann series) by rewriting Eq. (22) using these operators as

$$\tilde{\boldsymbol{\sigma}}=\tilde{\boldsymbol{\sigma}}_{\mathrm{Inc}}+i\omega\overline{\mathbf{H}}^{-1}\bar{\tilde{\boldsymbol{\eta}}}\tilde{\boldsymbol{\sigma}}\equiv\tilde{\boldsymbol{\sigma}}_{\mathrm{Inc}}+i\overline{\boldsymbol{\Omega}}\tilde{\boldsymbol{\sigma}}, \tag{23}$$

where $\overline{\boldsymbol{\Omega}}\equiv\omega\overline{\mathbf{H}}^{-1}\bar{\tilde{\boldsymbol{\eta}}}$, and then by applying Eq. (23) recursively to itself as

$$\tilde{\boldsymbol{\sigma}}=[\overline{\mathbf{I}}+i\overline{\boldsymbol{\Omega}}+(i\overline{\boldsymbol{\Omega}})^2+\cdots]\tilde{\boldsymbol{\sigma}}_{\mathrm{Inc}}=(\overline{\mathbf{I}}-i\overline{\boldsymbol{\Omega}})^{-1}\tilde{\boldsymbol{\sigma}}_{\mathrm{Inc}}. \tag{24}$$

$\overline{\mathbf{I}}$ is the identity operator. If the scattering is weak so that the stress field on the fracture can be approximated by the stress introduced by the incident wave, the (first-order) Born approximation can be used in Eq. (23), resulting in

$$\tilde{\boldsymbol{\sigma}}=\tilde{\boldsymbol{\sigma}}_{\mathrm{Inc}}+i\overline{\boldsymbol{\Omega}}\tilde{\boldsymbol{\sigma}}_{\mathrm{Inc}}=(\overline{\mathbf{I}}+i\overline{\boldsymbol{\Omega}})\tilde{\boldsymbol{\sigma}}_{\mathrm{Inc}}, \tag{25}$$

which can also be obtained by keeping the first two terms in the Neumann series (Born series) in Eq. (24). It is noted that an alternative approximation that is valid for the strong-scattering limit can be obtained if the stiffness of the fracture, instead of compliance, is used. The derivation of this approximation is shown in the Appendix.

Introducing higher-order terms in the Born series increases the applicable range of the approximation for stronger scattering, as long as the series is convergent. However, the series may converge very slowly, or even may not converge for moderately to strongly scattering fractures (for weakly to moderately scattering fractures if the formulation in Appendix is used). For these cases, the original system equation (19) has to be solved numerically.

B. Numerical analysis

In order to solve the integral equation (19) numerically, the equation is discretized in wave number to obtain a linear system of equations by applying the discrete Fourier transforms instead of the continuous Fourier transforms. This indicates that both the two-dimensional fracture compliance distribution and the resulting waves are treated as periodic, though the waves are periodic in the dynamic sense as in the Floquet boundary condition (i.e., a phase shift is included in the periodic boundary condition). Also, for the linear system of equations to be finite in size, the spectra of the transformed fracture compliance need to be band limited (decay away from the origin sufficiently fast). The discrete form of Eq. (19) is [for computational efficiency, Eqs. (22) and (23) are not used]

$$\begin{aligned}&\sum_{m'=0}^{M-1}\sum_{n'=0}^{N-1}[(i\omega)^{-1}\delta_{mm'}\delta_{nn'}\mathbf{H}_{mn}-\tilde{\boldsymbol{\eta}}_{m-m',n-n'}]\tilde{\boldsymbol{\sigma}}_{m'n'}\\&\quad=(i\omega)^{-1}\mathbf{H}_{mn}\tilde{\boldsymbol{\sigma}}_{\mathrm{Inc},mn}\\&\qquad(m=0,1,\ldots,M-1\quad\text{and}\quad n=0,1,\ldots,N-1).\end{aligned} \tag{26}$$

$\delta_{mm'}$ and $\delta_{nn'}$ are the Kronecker deltas. All vectors and matrices are evaluated at discrete wave numbers, $k_{xm}=2m\pi/L_x$ and $k_{yn}=2n\pi/L_y$, with indices m and n. Note that all these indices are periodic with periods M and N, and the compliance distribution is spatially periodic with periods L_x and L_y. The length of the periods given by M and N should be sufficiently long to avoid spectral leakage in the solution. By grouping the two indices (m,n) and (m',n') to the vectors and matrices into single indices l and l' $(l,l'=0,1,\ldots,MN-1)$, respectively, Eq. (26) are assembled into a single matrix equation

$$[(i\omega)^{-1}\overline{\mathbf{H}}-\bar{\tilde{\boldsymbol{\eta}}}]\overline{\boldsymbol{\sigma}}=(i\omega)^{-1}\overline{\mathbf{H}}\overline{\boldsymbol{\sigma}}_{\mathrm{Inc}}, \tag{27}$$

where

$$
\overline{\mathbf{H}} \equiv \begin{bmatrix} \mathbf{H}_0 & & & \\ & \mathbf{H}_1 & & \\ & & \ddots & \\ & & & \mathbf{H}_{MN-1} \end{bmatrix},
$$

$$
\bar{\bar{\boldsymbol{\eta}}} \equiv \begin{bmatrix} \tilde{\boldsymbol{\eta}}_0 & \tilde{\boldsymbol{\eta}}_{-1} & \cdots & \tilde{\boldsymbol{\eta}}_{-MN+1} \\ \tilde{\boldsymbol{\eta}}_{+1} & \tilde{\boldsymbol{\eta}}_0 & \cdots & \tilde{\boldsymbol{\eta}}_{-MN+2} \\ \vdots & \vdots & \ddots & \vdots \\ \tilde{\boldsymbol{\eta}}_{MN-1} & \tilde{\boldsymbol{\eta}}_{MN-2} & \cdots & \tilde{\boldsymbol{\eta}}_0 \end{bmatrix},
$$

$$
\overline{\boldsymbol{\sigma}} = \begin{bmatrix} \tilde{\boldsymbol{\sigma}}_0 \\ \tilde{\boldsymbol{\sigma}}_1 \\ \vdots \\ \tilde{\boldsymbol{\sigma}}_{MN-1} \end{bmatrix}, \quad \overline{\boldsymbol{\sigma}}_{\mathrm{Inc}} = \begin{bmatrix} \tilde{\boldsymbol{\sigma}}_{\mathrm{Inc},0} \\ \tilde{\boldsymbol{\sigma}}_{\mathrm{Inc},1} \\ \vdots \\ \tilde{\boldsymbol{\sigma}}_{\mathrm{Inc},MN-1} \end{bmatrix}. \tag{28}
$$

$\overline{\mathbf{H}}$ and $\bar{\bar{\boldsymbol{\eta}}}$ here are the inverse of multiplication operator $\overline{\mathbf{H}}^{-1}$ and convolution operator $\bar{\bar{\boldsymbol{\eta}}}$ in Eq. (23), respectively, defined for a finite number of wave numbers. Once the stress vector $\overline{\boldsymbol{\sigma}}$ is determined, by solving Eq. (27), the coefficient vectors for each wave number and wave mode component are computed via

$$
\mathbf{a}_{mn}^{+} = (i\omega \mathbf{S}_{mn}^{+})^{-1} \tilde{\boldsymbol{\sigma}}_{mn}, \tag{29}
$$

$$
\mathbf{a}_{mn}^{-} = (i\omega \mathbf{S}_{mn}^{-})^{-1} (\tilde{\boldsymbol{\sigma}}_{mn} - \tilde{\boldsymbol{\sigma}}_{\mathrm{Inc}}), \tag{30}
$$

for transmitted and reflected waves, respectively. From these, the displacement vectors for the transmitted and reflected waves are

$$
\mathbf{u}^{+}(x,y;z>0) = \sum_{m=0}^{M-1} \sum_{n=0}^{N-1} \mathbf{U}_{mn}^{+} \mathbf{E}_{mn}^{+} \mathbf{a}_{mn}^{+} e^{i(k_{xm}x + k_{yn}y - \omega t)}, \tag{31}
$$

$$
\mathbf{u}^{-}(x,y;z<0) = \sum_{m=0}^{M-1} \sum_{n=0}^{N-1} (\mathbf{U}_{mn}^{-} \mathbf{E}_{mn}^{-} \mathbf{a}_{mn}^{-} + \mathbf{U}_{mn}^{+} \mathbf{E}_{mn}^{+} \mathbf{a}_{\mathrm{Inc},mn}) e^{i(k_{xm}x + k_{yn}y - \omega t)}, \tag{32}
$$

where $\mathbf{E}_{mn}^{\pm} = \mathbf{E}^{\pm}(k_{mx}, k_{ny}; z)$ are the discrete forms of the phase-shift matrices defined in Eq. (8).

C. Computational considerations

The system matrix has a size $M_{\mathrm{mat}} \times M_{\mathrm{mat}}$ where $M_{\mathrm{mat}} = M \times N \times \mathrm{DOF}$ (degrees of freedom, three for three-dimensional problems) which grows rapidly as the number of wave number components increases. However, unique properties of the equation allow an efficient implementation of the method in a computer program, which leads to significant savings in the computer time and memory.

First, we discuss the memory considerations. From Eqs. (26), (27), and (28), notice that the system matrix consists of two parts: the 3×3 block diagonal part $\overline{\mathbf{H}}$, and the fully populated part $\bar{\bar{\boldsymbol{\eta}}}$. The latter matrix has the same structure as the Toeplitz matrix: each element of the matrix, a 3×3 submatrix, appears recursively, with the first entry of the compliance matrix $\tilde{\boldsymbol{\eta}}_{00} = \tilde{\boldsymbol{\eta}}_0$ in the diagonal. This is the direct consequence of expressing a convolution operation with a periodic function using a matrix. Therefore, for this system matrix, if an iterative solver such as the stabilized biconjugate gradient method[19] or the GMRES method[20] is used, it is sufficient to store only the block diagonal part of the matrix $\mathbf{H}$ and the transformed fracture compliance matrices corresponding to the first $3\times M_{\mathrm{mat}}$ part of the matrix $\bar{\bar{\boldsymbol{\eta}}}$.

An iterative solver requires both fast computation of matrix-vector products (mat-vecs) and effective preconditioning of the system matrix. The fully populated structure of the system matrix is usually not suited for fast computation of mat-vecs. Fortunately, Eq. (26) reveals that the matrix-vector product between $\bar{\bar{\boldsymbol{\eta}}}$ and $\overline{\boldsymbol{\sigma}}$ is essentially a single convolution between $\tilde{\boldsymbol{\eta}}_{m,n} (= \tilde{\boldsymbol{\eta}}_l)$ and $\tilde{\boldsymbol{\sigma}}_{m,n} (= \tilde{\boldsymbol{\sigma}}_l)$. Therefore, this computation can be carried out efficiently by transforming the vectors to the spatial domain and then transforming back the products between the vectors and the local compliance matrices to the wave number domain, using fast Fourier transforms. The preconditioning of the matrix is carried out in the spatial domain using the Kirchhoff approximation of the scattered waves. This involves first computing the scattering matrix for the incident plane wave at each location on the fracture, assuming the fracture is homogeneous and the compliance distribution is uniform. Subsequently, the resulting 3×3 block diagonal matrix is transformed in the wave number domain, and then LU decomposition is applied to the band-diagonal part of the matrix using a small bandwidth (3–9 are used). This LU-decomposed matrix is used for preconditioning the system matrix during each mat-vec operation.

Finally, for a plane incident wave with a wave number vector $(k_x^{\mathrm{Inc}}, k_y^{\mathrm{Inc}})$, the definition of the wave numbers is changed to $(k_{xm}, k_{yn}) = (k_x^{\mathrm{Inc}} + 2m\pi/L_x, k_y^{\mathrm{Inc}} + 2n\pi/L_y)$, so that the nonspecular wave number components close to the incident wave wave number are preferentially used to represent the scattered waves. This is a reasonable choice because the partial waves with wave numbers close to the source wave number are more strongly excited due to the coupling introduced by the diagonally dominant kernel of the convolution integral in Eq. (22). The expression for the stress vector also changes as

$$
\tilde{\boldsymbol{\sigma}}_{\mathrm{Inc},mn} \rightarrow \delta_{m0} \delta_{n0} \tilde{\boldsymbol{\sigma}}_{\mathrm{Inc}}. \tag{33}
$$

III. EXAMPLES

A. Comparison with a boundary element code

In order to check the performance of the numerical technique, we compared the numerical results of the wd-SDD technique developed in the preceding sections to the results from a two-dimensional, frequency-domain elastodynamic boundary element (BE) method of Hirose and Kitahara (1991).[21] In this test, the results from the two methods were compared for an incident plane P wave propagating in the z direction. For the wd-SDD, we assumed a fracture with sinusoidal compliance distribution, $\boldsymbol{\eta}(x,y) = \eta_0 \mathbf{I}(1 - \cos 2\pi x/\lambda)/2$ where $\mathbf{I}$ is a 3×3 identity matrix, $\eta_0 = 1.33 \times 10^{-10}$ m/Pa, and period $\lambda = 4$ m. In contrast, the two-dimensional fracture in the BE model is finite in extent from -28 m to $+28$ m.

z-direction displacement waveforms computed for receivers located on both sides of the fracture are shown in Fig.

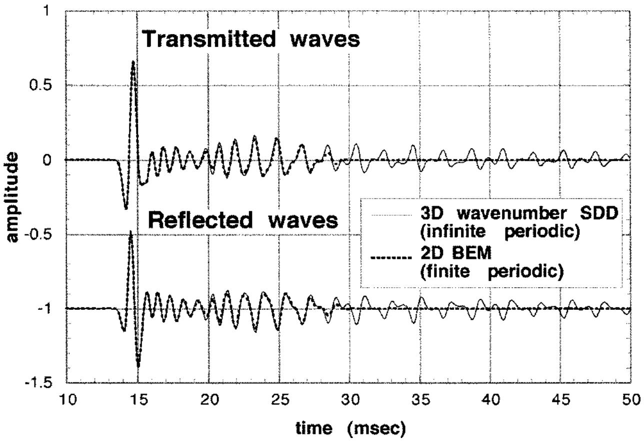

FIG. 2. Comparison between waveforms computed using the BEM and the wd-SDD method. A plane *P* wave is normally incident on the fractures. The first-arriving parts of the waves show very good agreement. The results of the wd-SDD method show long-lasting reverberations ("coda") due to the waves scattered a long distance away from the receiver.

2. The distance of the receivers from the fracture is 20 m, the incident wave is a plane *P* wave Ricker wavelet (second derivative of a Gaussian wavelet) with a central frequency corresponding to 4 m which is also the spatial period of the compliance distribution. Compared to the SDD results, the BE results show much shorter, more compact waveforms, because the fracture in the BE model is finite. However, the waveforms are in good agreement until about 28 ms, for both reflected and transmitted waveforms, which indicates that the scattering of the waves can be accurately modeled using the wave-number-domain SDD technique. The secondary arrivals that also show rather good agreement are due to the *S* waves converted by the fracture.

B. Numerical models of a heterogeneous fracture

In the following examples, we used a fracture with a numerically simulated stochastic compliance distribution. For simplicity, the fracture compliance matrix was assumed to be proportional to an identity matrix, i.e., normal and shear compliances are the same, and $\boldsymbol{\eta}(x,y)=\eta(x,y)\mathbf{I}$. A distribution of logarithmic compliance, $\ln \eta(x,y)$, was generated from a Gaussian correlation function with a correlation length (one standard deviation) of 4 m and uncorrelated phase between the Fourier components.[22] The range of a single periodic cell is $(L_x,L_y)=(64\,\mathrm{m},64\,\mathrm{m})$. The resulting compliance $\eta(x,y)$, shown in Fig. 3, has a log-normal distribution with a mean and a standard deviation of the compliance of 6.74×10^{-11} m/Pa and 4.87×10^{-11} m/Pa, respectively. The correlation length of the distribution (one standard deviation of a fitted Gaussian profile) is approximately 4 m.

C. Exact solutions

Waves scattered by the heterogeneous fracture in Fig. 3 were computed for a plane incident *P* wave, using a Ricker wavelet (second derivative of a Gaussian function) with a central frequency, 750 Hz, corresponding to the correlation length of the fracture. The velocities and density of the ho-

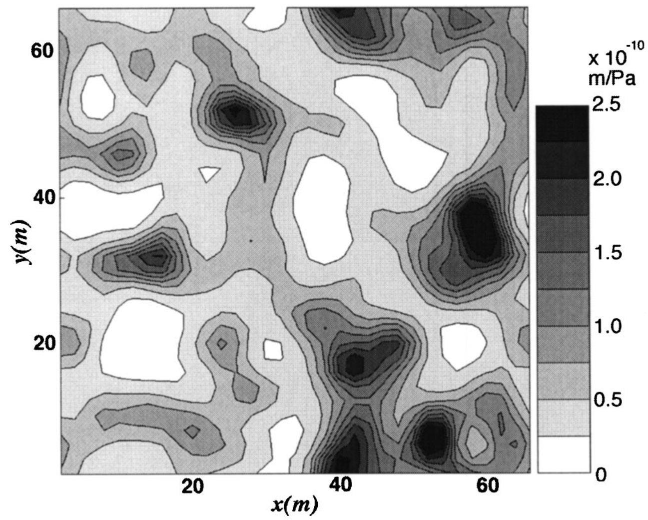

FIG. 3. Single periodic cell for the compliance distribution of a simulated fracture. The distribution is periodic in both *x* and *y* directions. The correlation length of the distribution is 4 m (single standard deviation of a fitted Gaussian distribution), and the compliance values vary by about an order of magnitude.

mogeneous, isotropic, elastic background were $c_p=3000$ m/s, $c_s=1731$ m/s, and $\rho=2100$ kg/m^3, respectively. If the fracture had a homogeneous fracture compliance distribution, the mean compliance value of 6.74×10^{-11} m/Pa would give the same normal incidence *P* wave transmission and reflection coefficients of amplitudes of $\sqrt{2}/2\sim0.71$. The condition for this to occur is that frequency$=\rho c_p/\pi$.

The snapshots in Figs. 4(a) and 4(b) were computed for both a normally incident *P* wave and an obliquely incident *P* wave with a unit propagation vector $(v_x,v_y,v_z)=(1/\sqrt{3},1/\sqrt{3},1/\sqrt{3})$, respectively. To emphasize the scattered waves with small amplitudes, the amplitude scale was magnified by a factor of 4, which caused the saturation of scale for a part of transmitted and reflected waves. In both snapshots, it can be seen that patches of large and small compliance scatter the incident waves, creating circular (spherical) diffraction patterns in both sides of the fracture. For the normal incidence case, the amplitude and phase fluctuations in the both transmitted and reflected waves can be seen. It is also noted that incoherent *S* waves were generated. For the oblique incidence case, the diffracted waves generated horizontally propagating *P* waves in later times, part of which was critically refracted as head waves propagating away from the fracture (multiple, faint oblique wave fronts propagating symmetrically across the fracture).

Figure 5 shows the amplitude distribution of individual wave number components for a given frequency (750 Hz) and angles of incidence (normal and oblique) of incident plane *P* waves. The axes of the plots show the integral numbers (m,n) corresponding to the wave number components $(k_{xm},k_{yn})=(k_x^{\mathrm{Inc}}+2m\pi/L_x,k_y^{\mathrm{Inc}}+2n\pi/L_y)$. Remember that the components of wave numbers used in the numerical simulations were distributed around the incident wave number $(k_x^{\mathrm{Inc}},k_y^{\mathrm{Inc}})$. These diagrams can be used to see if the spectrum leakage occurs due to a premature truncation of the wave number series (or undersampling in the spatial do-

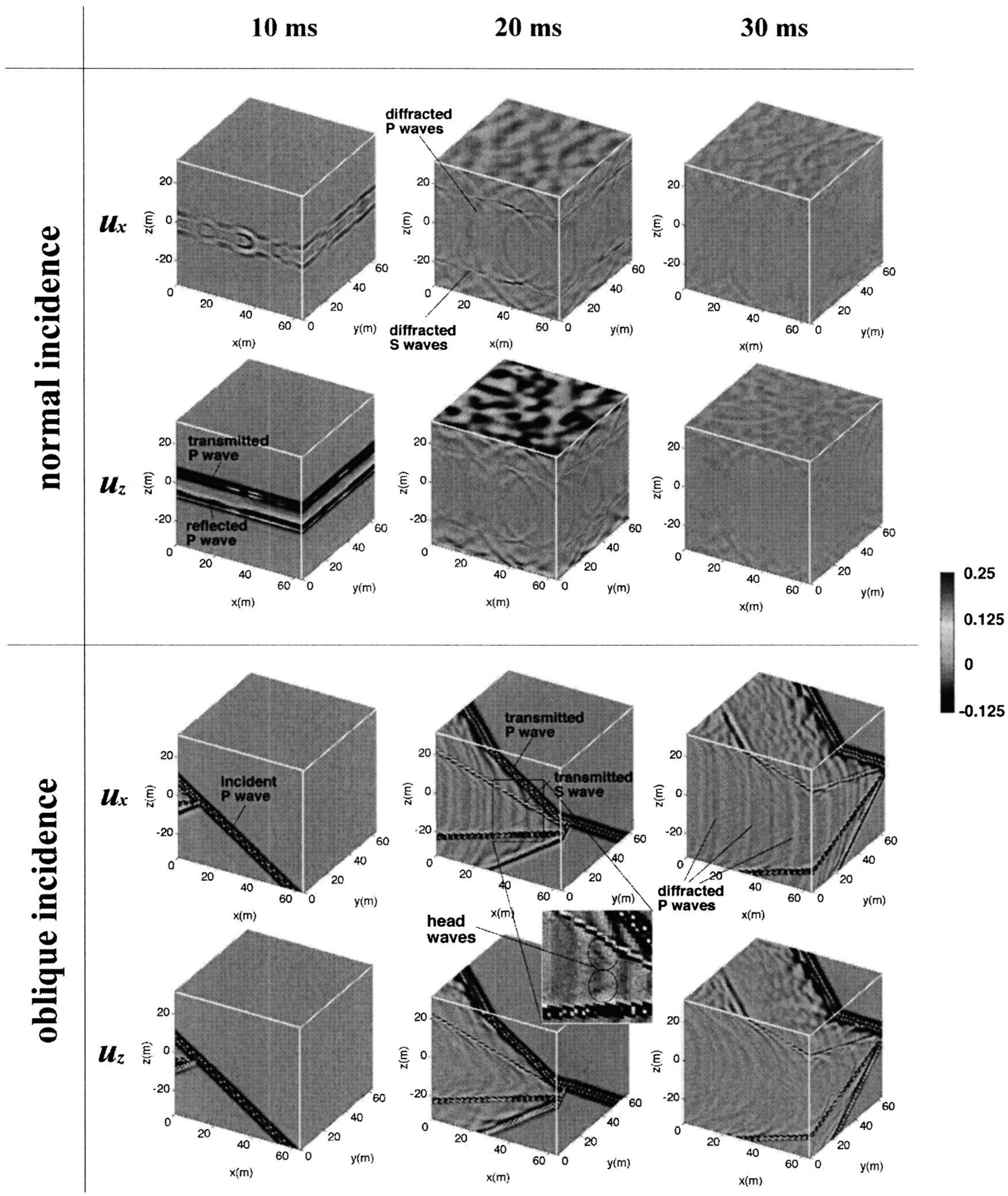

FIG. 4. Three-dimensional snapshots of the waves scattered by a single plane fracture at $z=0$, with the heterogeneous fracture compliance distribution shown in Fig. 4. Both x and z direction particle displacements are shown on the surfaces of a cube cut out of an infinite medium containing the fracture. The top two rows are for a normally incident P wave propagating from the bottom of the plots, and the bottom two rows are for an obliquely incident P waves propagating from the bottom left corner of the cube, in the $(1/\sqrt{3},1/\sqrt{3},1/\sqrt{3})$ direction.

main). For this example, although the length of the wave number series was rather short $[(\mathrm{M},\mathrm{N})=(32,32)]$, the amplitudes of the scattered waves became significantly small at the edge of the diagram, showing *a posteori* that the selected length of the series was sufficiently long. It is also noted that while the normal-incidence case showed no coupling between the incident P wave and Sh waves, the oblique-incidence case showed small Sh waves.

D. Born approximations and low- and high-frequency asymptotic solutions

If the compliance distribution is uniform, only the specular wave number component needs to be examined. This is because the convolution matrix, $\bar{\bar{\boldsymbol{\eta}}}$, and therefore the system matrix in Eq. (27), becomes block diagonal due to the lack of coupling between different wave number components. For a plane incident wave, using the vectors and matrices in Eq. (28), the "exact" equation (27) reduces to

$$[(i\omega)^{-1}\mathbf{H}_0-\tilde{\boldsymbol{\eta}}_0]\tilde{\boldsymbol{\sigma}}=(i\omega)^{-1}\mathbf{H}_0\tilde{\boldsymbol{\sigma}}_{\mathrm{Inc}} \quad \text{or}$$

$$(\mathbf{I}-i\omega\mathbf{H}_0^{-1}\tilde{\boldsymbol{\eta}}_0)\tilde{\boldsymbol{\sigma}}_0\equiv(\mathbf{I}-i\boldsymbol{\Omega}_0)\tilde{\boldsymbol{\sigma}}_0=\tilde{\boldsymbol{\sigma}}_{\mathrm{Inc}}. \tag{34}$$

For a diagonal fracture compliance matrix $\tilde{\boldsymbol{\eta}}_0\equiv\mathrm{diag}[\eta_{xx},\eta_{yy},\eta_{zz}]$, $\boldsymbol{\Omega}_0$ is

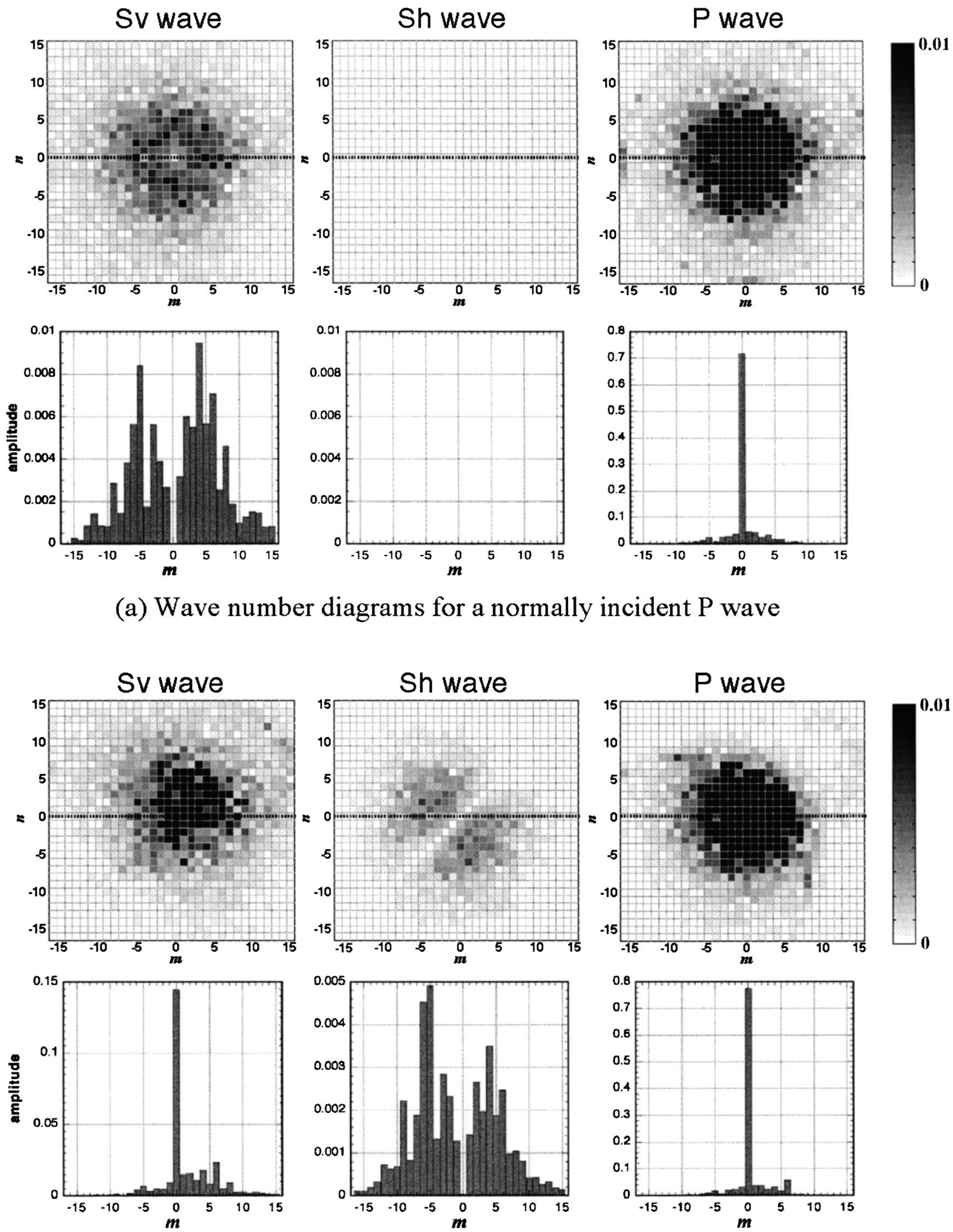

FIG. 5. Sv, Sh, and P-wave amplitude distributions of wave number components around a unit amplitude, incident P wave ($m=n=0$). Both the normal incidence case (a) and oblique incidence case (b) are shown. The frequency of the waves is 750 Hz. The color scale is saturated for components with an amplitude larger than 0.01. The line diagrams are the profiles of the distributions cut along the line, $m=0$ (shown as a dotted line). The amplitudes of the wave number components decay quickly away from the center (incident wave).

$$\mathbf{\Omega}_0=\mathrm{Diag}\left[\frac{\omega\rho c_S\eta_{xx}}{2}\ \frac{\omega\rho c_S\eta_{yy}}{2}\ \frac{\omega\rho c_P\eta_{zz}}{2}\right]$$
$$\equiv\mathrm{Diag}[\Omega_{Sv}\ \ \Omega_{Sh}\ \ \Omega_P]. \tag{35}$$

Therefore the components of this matrix are the dimensionless frequencies defined by Haugen and Schoenberg (2000).[23] The stiffness based equations (defined in Appendix) also reduces to

$$(i\omega\mathbf{H}_0^{-1}-\tilde{\boldsymbol{\kappa}}_0)[\tilde{\mathbf{u}}]=i\omega\mathbf{H}_0^{-1}[\tilde{\mathbf{u}}]_{\mathrm{Inc}}\quad\text{or}$$

$$[\mathbf{I}-(i\omega)^{-1}\mathbf{H}_0\tilde{\boldsymbol{\kappa}}_0][\tilde{\mathbf{u}}]_0\equiv(\mathbf{I}+i\mathbf{T}_0)[\tilde{\mathbf{u}}]_0=[\tilde{\mathbf{u}}]_{\mathrm{Inc}}. \tag{36}$$

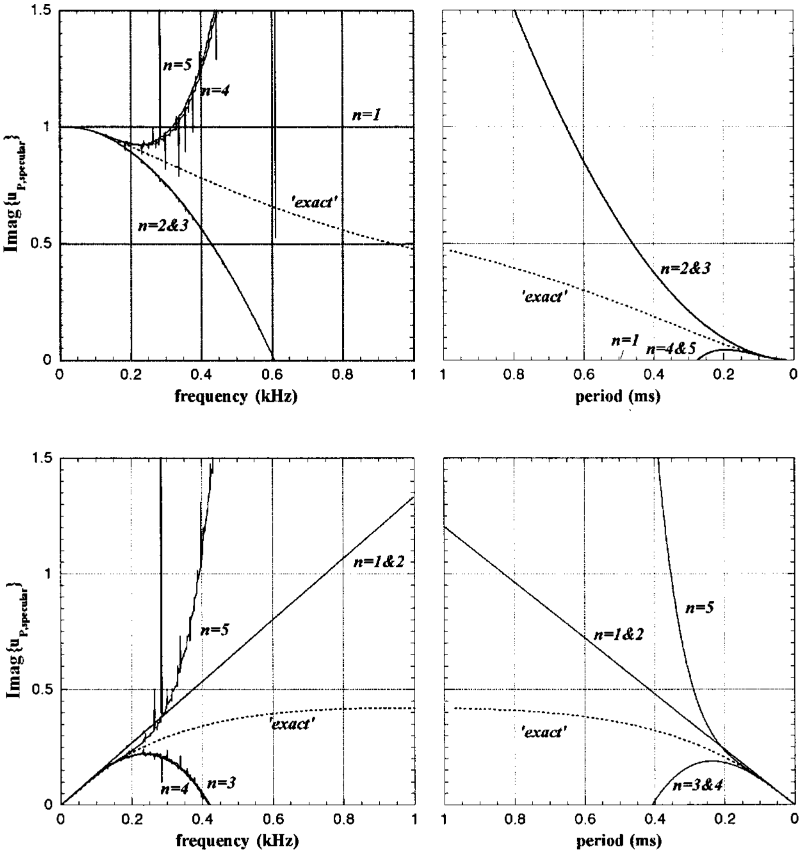

FIG. 6. Real (top) and imaginary (bottom) parts of the transmission coefficients (the most dominant specular components of P wave are compared) computed using the Born approximations of different orders up to $n=5$. For comparison, the "exact" numerical solutions are also plotted. The low-frequency (left) approximations are computed using the compliance-based Born series while the high-frequency (right) approximations are obtained from the stiffness-based Born series.

Since both $\tilde{\boldsymbol{\eta}}_0$ and $\tilde{\boldsymbol{\kappa}}_0$ are constant and diagonal, and $\mathbf{H}_0$ is also diagonal for normally incident waves, $\tilde{\boldsymbol{\kappa}}_0=\tilde{\boldsymbol{\eta}}_0^{-1}$, and $\mathbf{T}_0=\boldsymbol{\Omega}_0^{-1}$. Therefore, the two Born series are

$$\tilde{\boldsymbol{\sigma}}_0=\sum_{n=0}^{\infty} i^n \boldsymbol{\Omega}_0^n \cdot \tilde{\boldsymbol{\sigma}}_{\mathrm{Inc}}, \tag{37}$$

$$[\tilde{\mathbf{u}}]_0=\sum_{n=0}^{\infty} (-i)^n \boldsymbol{\Omega}_0^{-n} \cdot [\tilde{\mathbf{u}}]_{\mathrm{Inc}}. \tag{38}$$

Since the eigenvalues of the matrices $\boldsymbol{\Omega}_0$ and $\boldsymbol{\Omega}_0^{-1}$ are the Haugen and Schoenberg's dimensionless frequencies and their inverse, the above Born series converge for $|\Omega_{Sv,Sh,P}|<1$ for compliance based series, and $|\Omega_{Sv,Sh,P}|>1$ for the stiffness based series. Therefore compliance and stiffness-based Born approximations can be applied in the low- and high-frequency limits, respectively. Physically, the compliance-based Born series can be viewed as a perturbation of the totally transmitted waves across a welded fracture in the static limit by small reflection of nonzero-frequency wave energy. In contrast, the stiffness-based Born series is a perturbation of the totally reflected waves for an open fracture in the high-frequency limit by small transmission of finite-frequency wave energy.

For heterogeneous fracture compliance and stiffness distributions, these relationships are more complicated due to the nonspecular scattering of waves. The matrix-vector form of the Born series is obtained from Eq. (23) as

$$\bar{\boldsymbol{\sigma}}=\sum_{n=0}^{\infty} (i\omega\bar{\mathbf{H}}^{-1}\bar{\bar{\boldsymbol{\eta}}})^n \bar{\boldsymbol{\sigma}}_{\mathrm{Inc}} \equiv \sum_{n=0}^{\infty} i^n \bar{\boldsymbol{\Omega}}^n \bar{\boldsymbol{\sigma}}_{\mathrm{Inc}}. \tag{39}$$

Also, from the Appendix, the stiffness-based Born series is

$$[\bar{\mathbf{u}}]=\sum_{n=0}^{\infty} [(i\omega)^{-1}\bar{\mathbf{H}}\bar{\bar{\boldsymbol{\kappa}}}]^n [\bar{\mathbf{u}}]_{\mathrm{Inc}} \equiv \sum_{n=0}^{\infty} (-i)^n \bar{\mathbf{T}}^n [\bar{\mathbf{u}}]_{\mathrm{Inc}}. \tag{40}$$

These series are convergent if $\|\bar{\boldsymbol{\Omega}}\|<1$ and $\|\bar{\mathbf{T}}\|<1$, i.e., the magnitude of the eigenvalues of the matrices are smaller than unity. It is desirable to interpret these conditions as the low- and high-frequency limits, as we saw for a homogeneous fracture, so that we can apply the Born approximations to the low- and high-frequency scattering problems for a heterogeneous fracture. We will examine these possibilities using numerical simulations.

For the fracture model used in the preceding section, we can compute the scattered wavefield from the (generalized) Born series. For simplicity, we assume normally incident, monochromatic transmitted P waves, and examine only the specular component of the waves. The "exact" solutions are also computed from Eq. (27) for a range of frequencies, and compared to the Born approximations of different orders. Figures 6 shows the comparisons of transmission coefficient amplitudes computed from the z-direction particle motions of P waves. Each curve in the plots is labeled with the order of Born approximation. The low-frequency approximations were computed using the compliance-based Born series, and the high-frequency approximations were computed using the stiffness-based Born series. As can be seen from the plots, the Born approximations appear to be valid in both low- and high-frequency limits, respectively, and including higher-order terms in the Born series does improve the applicability

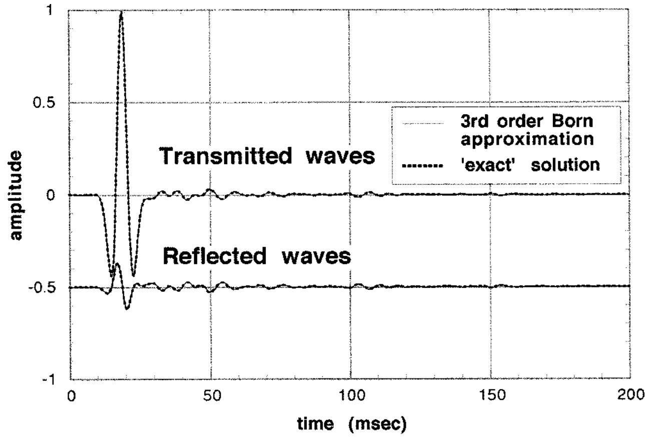

FIG. 7. Comparison between z-direction particle motions computed by solving the matrix equation in Eq. (27) and by the third-order, compliance-based Born approximation. The central frequency of the incident Ricker wavelet (P wave) is 100 Hz, and the receivers are located on both sides, 32 m away from the fracture. The results are nearly identical.

of the approximations. For the fracture and background properties used for this example, the low-frequency approximation is valid below 150 Hz, and the high-frequency approximation is valid above 10 kHz. In Fig. 7, z-direction particle displacements are compared for both third-order Born approximation and the exact numerical solution. The receivers are located at $z=32\,\mathrm{m}$ (transmitted waves) and $z=-32\,\mathrm{m}$ (reflected waves), and a low frequency (a central frequency of 100 Hz) Ricker wavelet was used. For this example, the results of the two methods are indistinguishable.

However, these results do not necessarily guarantee that the first two terms in the Born series (first-order Born approximations) are exactly the leading terms in the series, i.e., low- and high-frequency asymptotes of the exact solutions. We examined the low- and high-frequency limit behavior of the two Born series more in detail by plotting the displacement amplitudes computed from the individual terms of both series as a function of frequency [Figs. 8 left and right, respectively]. It is noted that the lowest order term of the stiffness-based Born series is $O(1/\omega)$, because the transmitted wave's displacement computed from the displacement is computed via a relationship $\tilde{\mathbf{u}}^{+}=[\tilde{\mathbf{u}}]-[\tilde{\mathbf{u}}]_{\mathrm{Inc}}$ which removes the 0th order term from the original Born series.

From Fig. 8 left, the second and the higher-order terms of the compliance-based Born series all exhibit $O(\omega)$ dependence, instead of the expected $O(\omega^n)$ dependence for a homogeneous fracture in Eq. (37), where n is the order of the term. This indicates that, although it is still a good approximation due to small magnitudes of the terms higher than $n>2$, the compliance-based Born approximation does not give the exact low-frequency asymptotic solution. In contrast, from Fig. 8 right, the terms in the stiffness-based Born approximation are $O(1/\omega^n)$, giving correct high-frequency asymptotes.

Since the frequency-independent $\mathbf{H}$ matrices should result in $O(\omega^n)$ dependence of the compliance-based Born series from Eq. (39), the above result seems to be incorrect. This apparent discrepancy is due to the wave number convolution involving both $\mathbf{H}=\mathbf{H}(k_r/\omega)$ and $\tilde{\boldsymbol{\eta}}=\tilde{\boldsymbol{\eta}}(k_r)$ for twice or more scattered waves in the compliance-based Born series. $\mathbf{H}$ is frequency independent only if the plane parallel wave number k_r is viewed as a function of frequency ($k_r/\omega=p$, p is the plane parallel slowness). However, this exchange of independent variables does not make the convolution integral frequency independent, because $\tilde{\boldsymbol{\eta}}$, which originally is dependent upon only k_r, is now frequency dependent: $\tilde{\boldsymbol{\eta}}=\tilde{\boldsymbol{\eta}}(k_r)=\tilde{\boldsymbol{\eta}}(\omega p)$. Therefore, the resulting convolution operators (or matrices) $\underline{\boldsymbol{\Omega}}^n\equiv(\omega\underline{\mathbf{H}}^{-1}\underline{\tilde{\boldsymbol{\eta}}})^n$ are not $O(\omega^n)$. In contrast, for high-frequencies and the stiffness-based Born series, $\mathbf{H}$ is frequency independent without exchanging the variables, because $\mathbf{H}=\mathbf{H}(k_r/\underline{\omega})=\mathbf{H}(k_z^P/k_S, k_z^S/k_S)\rightarrow\mathbf{H}(c_S/c_P,1)$, which yields $\underline{\mathbf{T}}^n\sim O(\omega^{-n})$.

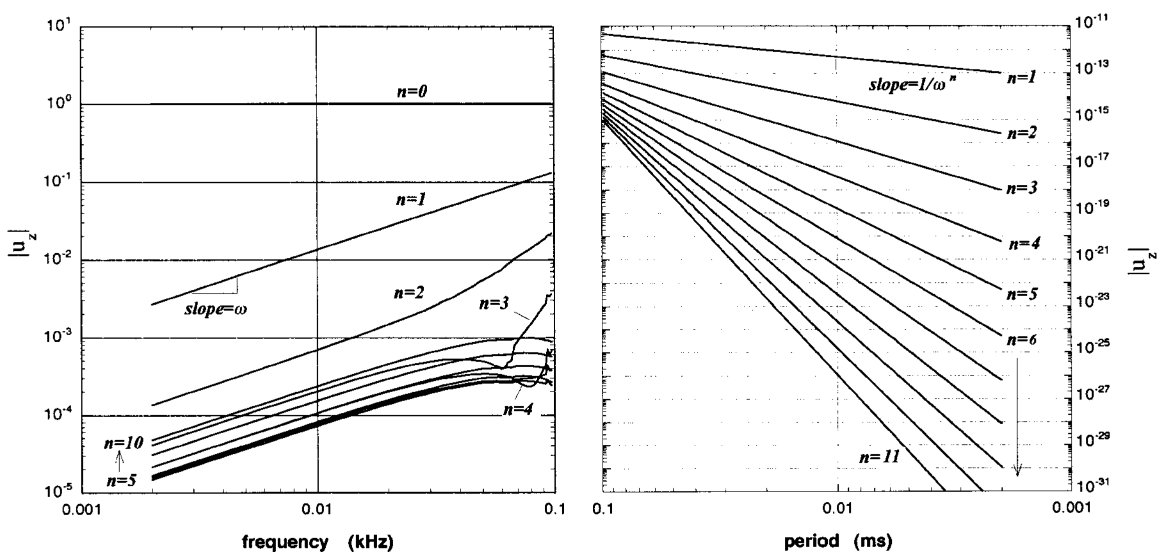

FIG. 8. Displacement amplitude computed from individual terms in the Born series for a unit-amplitude, plane incident P wave. The z-direction particle displacements of transmitted P wave are shown. The nth-order term of the high-frequency Born series (right) scales as $O(1/\omega^n)$. In contrast, all the terms except for the 0th-order term (incident wave) in the low-frequency Born series (left) scale as $O(\omega)$. The absolute magnitudes of the higher order terms, however, are small for this example.

IV. CONCLUSIONS

We developed a plane wave method to compute the three-dimensional scattering of plane elastic waves by a fracture with a heterogeneous stiffness (compliance) distribution. This technique allows us to examine the relationships between the characteristics of scattered elastic waves and the microstructural variations along the fracture plane (e.g., surface contact and crack distribution, gouge layer thickness variation) that are modeled as heterogeneities in the fracture compliance distribution.

This method is a straightforward extension of the commonly used seismic displacement discontinuity (SDD) method for a homogeneous fracture, to a fracture with a heterogeneous fracture compliance distribution. Even though the developed technique is a full-waveform technique and successfully models a variety of wave phenomena involving a fracture, such as mode converted waves, head waves (refracted waves), surface waves and diffracted waves, it does not require massive parallel computers as finite difference methods and boundary element methods would do.

The current numerical technique can be applied to nonplanar incident waves by simply modifying the incident wave vector. In this case, however, a larger number of wave number components need to be used in the matrix equation. It should also be noted that this technique is difficult to apply to extremely heterogeneous fractures, because such fractures typically results in a large linear system of equations to solve for nonspecular components of scattered waves with wave numbers far different from the incident wave. Further, the compliance-based equations break down for open cracks and voids (infinite compliance) and the stiffness-based equations break down for welded surfaces (infinite stiffness), because the Fourier transforms cannot be performed.

Last, we demonstrated that two types of Born series can be used to examine the low- and high-frequency limit behavior of the wave scattering by a heterogeneous fracture. The low-frequency Born series (compliance-based formulation), however, should be used with a caution, because the lowest-order term does not provide the exact low-frequency asymptotic solution. In contrast, the high-frequency Born series (stiffness-based formulation) is the exact high-frequency asymptote, although, in practice, the local SDD conditions used as a basis of the theory may not be valid for such high frequencies.

ACKNOWLEDGMENTS

This research has been supported by the Office of Science, Office of Basic Energy Sciences, Division of Chemical Sciences of the U.S. Department of Energy under Contract No. DE-AC76SF00098. Also, the authors would like to thank Dr. Michael Schoenberg for his helpful comments and suggestions.

APPENDIX

As an alternative to using the compliance-based equations, we can use equations based on fracture stiffness $\boldsymbol{\kappa}(x,y)=\boldsymbol{\eta}^{-1}(x,y)$. In this case, Eq. (7) in the text is replaced by

$$(\tilde{\boldsymbol{\kappa}}*[\tilde{\mathbf{u}}])(k_x,k_y)=\tilde{\boldsymbol{\sigma}}(k_x,k_y). \tag{A1}$$

$\tilde{\boldsymbol{\kappa}}$ is the Fourier transformed fracture stiffness matrix. By using the displacement discontinuity vector $[\tilde{\mathbf{u}}]$ as the primary variable, the traction vector $\tilde{\sigma}$ is eliminated from Eq. (A1), resulting in

$$(i\omega\mathbf{H}^{-1}-\tilde{\boldsymbol{\kappa}}*)[\tilde{\mathbf{u}}]=i\omega\mathbf{H}^{-1}[\tilde{\mathbf{u}}]_{\mathrm{Inc}}, \tag{A2}$$

where the incident term for the displacement–discontinuity vector is defined as

$$[\tilde{\mathbf{u}}]_{\mathrm{Inc}}\equiv-\mathbf{HS}^{+}\mathbf{a}_{\mathrm{Inc}}. \tag{A3}$$

Equation (A3) is the displacement–discontinuity vector for an open fracture (free surface). The integral equation corresponding to Eq. (22) is

$$\begin{aligned}[\tilde{\mathbf{u}}](k_x,k_y)&=[\tilde{\mathbf{u}}]_{\mathrm{Inc}}(k_x,k_y)+(i\omega)^{-1}\mathbf{H}(k_x,k_y)\\&\quad\times\int_{-\infty}^{+\infty}\int_{-\infty}^{+\infty}\tilde{\boldsymbol{\kappa}}(k_x-k_x',k_y-k_y')[\tilde{\mathbf{u}}]\\&\quad\times(k_x',k_y')\,dk_x'\,dk_y',\end{aligned} \tag{A4}$$

and the Neumann series (Born series) corresponding to Eq. (24) is

$$[\tilde{\mathbf{u}}]=[\overline{\mathbf{I}}-i\overline{\mathbf{T}}+(-i\overline{\mathbf{T}})^2+\cdots][\tilde{\mathbf{u}}]_{\mathrm{Inc}}=(\overline{\mathbf{I}}+i\overline{\mathbf{T}})^{-1}[\tilde{\mathbf{u}}]_{\mathrm{Inc}}, \tag{A5}$$

where the operator $\overline{\mathbf{T}}$ is defined as $\overline{\mathbf{T}}\equiv\omega^{-1}\overline{\mathbf{H}}\bar{\tilde{\boldsymbol{\kappa}}}$. Note that, in general, the fracture stiffness convolution operator $\bar{\tilde{\boldsymbol{\kappa}}}$ is not the inverse of the compliance operator $\bar{\tilde{\boldsymbol{\eta}}}$. Equation (A4) can be written in a matrix form to be solved numerically. The resulting matrix equation is equivalent to the compliance-based equation (26) but shows faster convergence of iterative solutions at higher frequencies. This property can be used to efficiently implement the computer program to solve for the "exact" solutions: the compliance formulation is used at low frequencies and the stiffness formulation at high frequencies.

[1] E. Liu, J. A. Hudson, and T. Pointer, "Equivalent medium representation of fractured rock," J. Geophys. Res., [Solid Earth] **105**, 2981–3000 (2000).

[2] M. A. Schoenberg, "Elastic wave behavior across linear slip interfaces," J. Acoust. Soc. Am. **68**, 1516–1521 (1980).

[3] J. Baik and R. B. Thompson, "Ultrasonic scattering from imperfect interfaces: a quasi-static model," J. Nondestruct. Eval. **4**, 177–196 (1984).

[4] Y. C. Angel and J. D. Achenbach, "Reflection and transmission of elastic waves by a periodic array of cracks," J. Appl. Mech. **52**, 33–41 (1985).

[5] L. R. Myer, D. Hopkins, and N. G. W. Cook, "Effects of contact area of an interface on acoustic wave transmission," Proceedings of the 26th US Symposium on Rock Mechanics, Rapid City, Ed.: E. Ashworth, Balkema, Rotterdam, Boston, 549–556 (1985).

[6] L. J. Pyrak-Nolte and N. G. W. Cook, "Elastic interface waves along a fracture," Geophys. Res. Lett. **14**, 1107–1110 (1987).

[7] S. I. Rokhlin and Y. J. Wang, "Analysis of boundary conditions for elastic wave interaction with an interface between two solids," J. Acoust. Soc. Am. **89**, 503 (1991).

[8] S. Nakagawa, K. T. Nihei, and L. R. Myer, "Elastic wave propagation along a set of parallel fractures," Geophys. Res. Lett., DOI 10 1029/2002 GLO14925 (2002).

[9] L. J. Pyrak-Nolte, L. R. Myer, N. G. W. Cook, and P. A. Witherspoon, "Hydraulic and mechanical properties of natural fractures in low permeability rock," Proceedings of the 6th International Congress of Rock Mechanics, Montreal, I, Eds: G. Herget and S. Vongpaisal, Balkema, Rotterdam, Boston, I, 225–232 (1987).

[10] O. Buck, D. K. Rehbein, and R. B. Thompson, "Crack tip shielding by

asperity contact as determined by acoustic measurements,'' Eng. Fract. Mech. **28**, 413 (1987).
[11] A. Oliger, L. J. Pyrak-Nolte, and D. D. Nolte, ''Scismic focusing by a single planar fracture,'' Geophys. Res. Lett. **30**, DOI 10 1029/2002GL014925 (2003).
[12] E. Hakami and E. Larsson, ''Aperture measurement and flow experiments on a single natural fracture,'' Int. J. Rock Mech. Min. Sci. Geomech. Abstr. **33**, 395–404 (1996).
[13] L. J. Pyrak-Nolte and D. D. Nolte, ''Frequency dependence of fracture stiffness,'' Geophys. Res. Lett. **19**, 325–328 (1992).
[14] K. T. Nihei, ''Modeling elastic waves in fractured rock with the Kirchhoff method,'' M.S. thesis, University of California at Berkeley, 1989.
[15] A. Oliger, L. J. Pyrak-Nolte, and D. D. Nolte, ''Seismic focusing by a single planar fracture,'' Geophys. Res. Lett. (in press).
[16] Y. Mikata and J. D. Achenbach, ''Interaction of harmonic waves with a periodic array of inclined cracks,'' Wave Motion **10**, 59–72 (1988).
[17] M. Punjani and L. J. Bond, ''Scattering of plane waves by a partially closed crack,'' Rev. Prog. Quant. Nondestr. Eval. **5A**, 61–71 (1986).
[18] R. T. Coates and M. A. Schoenberg, ''Finite-difference modeling of faults and fractures,'' Geophysics **60**, 1514–1526 (1995).
[19] H. Van der Vorst, ''Bi-CGSTAB: A fast and smoothly converging variant of Bi-CG for the solution of nonsymmetric linear equations,'' SIAM (Soc. Ind. Appl. Math.) J. Sci. Stat. Comput. **13**, 631–644 (1992).
[20] Y. Saad and M. H. Schultz, ''GMRES: A generalized minimum residual algorithm for solving unsymmetric linear systems,'' SIAM (Soc. Ind. Appl. Math.) J. Sci. Stat. Comput. **7**, 856–869 (1986).
[21] S. Hirose and M. Kitahara, ''Scattering of elastic waves by a crack with spring-mass contact,'' Int. J. Numer. Methods Eng. **31**, 789–801 (1991).
[22] E. Pardo-Iguzquiza and M. Chica-Olmo, ''The Fourier Integral Method: An efficient spectral method for simulation of random fields,'' Math. Geol. **25**, 177–217 (1993).
[23] G. U. Haugen and M. A. Schoenberg, ''The echo of a fault or fracture,'' Geophysics **65**, 176–189 (2000).